Fast and reliable flux map on cylindrical receivers

Francisco J. Collado*, Jesus Guallar

Department of Mechanical Engineering, EINA, Universidad de Zaragoza, María de Luna 3, 50018 Zaragoza, Spain

ABSTRACT

The thermal design of external solar receivers is a complex problem, in which the main input is the flux caused by the entire heliostat field on the cylindrical receiver surface. In this work, a fast and reliable model of flux distribution on the cylindrical receiver is proposed. This new cylinder flux map is based on the HFLCAL model for the analytic flux density sent by a heliostat on its image plane and the projection, in the direction of the central reflected ray, of any point in the plane image onto the cylindrical surface. The heliostat flux density includes shading and blocking, cosine of the incidence angle, atmospheric attenuation and effective reflectivity. A differential energy balance supports the coherence of the new model, i.e. the power contained in a differential of area in the image plane has to be equal to the power contained in the projected differential of area onto the cylinder. As an application of this new flux distribution on cylindrical receivers, we present the receiver sizing for a Noor III-like 150 MWe plant, with 7400 heliostats, in which the minimum LCOE gives the receiver diameter and a preliminary receiver height. With the help of the new flux map, this height is analysed to verify the maximum allowable flux. A multi-aiming strategy suggested by Vant-Hull (2002) and put into practice by Sanchez-Gonzalez and Santana (2015) is used to spread the hot spots along the receiver height. The PC CPU time to produce a coherent flux map on the cylinder is around six seconds.

1. Introduction

The solar power tower (SPT) is now almost a mature technology with several projects already operational at a commercial scale (> 100 MWe) or under development (NREL-SolarPACES, 2018), in which their projected levelized cost of energy (LCOE) is entering into competition with that of fossil-fuel power plants (New Energy Update, 2018). Many of these commercial-scale projects consist of an external cylindrical receiver atop the tower and a surrounding heliostat field. The design of these external receivers is critical for efficient plant operation and sufficient operational lifetimes (Boerema et al., 2013). The full solution of the heat-transfer problem of solar irradiated receiver tube walls filled with a heat-transfer fluid, usually molten salts, is rather complex. The flux map caused by thousands of heliostats is also connected with a precise heliostat field definition and an aiming strategy to avoid peak fluxes and hot spots. Therefore, the thermal design of these receivers is still an open question.

To address this complex problem, the receiver design begins with a given number of heliostats, largely equivalent to the plant's power, and a geographical location. First, optimising the collector field design involves selecting the heliostat field layout, tower optical height and receiver dimensions (diameter and height) with the lowest LCOE (see, for example, Singer et al., 2010; Collado and Guallar, 2016). The extensive

review of software for optical analysis and optimisation of heliostat fields recently performed by Cruz et al. (2017) would give an idea of the difficulty of efficiently managing thousands of heliostats. Second, a flux map of the solar energy reflected by the entire heliostat field onto the cylindrical receiver surface has to be calculated. Convolution methods work with models of the analytic heliostat flux density function, which is the result of the mathematical superposition of error cones, such as DELSOL3 (Kistler, 1986), HFLCAL (Schwarzbölz et al., 2009) or UNIZAR (Collado, 2010). The other option is Monte Carlo ray-tracing methods that trace a bundle of random rays from the sun, e.g. STRAL (Belhomme et al., 2009) or SolTrace (Wendelin et al., 2013). Recently, SolarPILOT (NREL-SolarPILOT, 2018) has even integrated these two options, i.e. it extends the DELSOL3 analytic flux density function, applying calculations to each heliostat image, and it also includes the SolTrace ray-tracing engine so that more complex geometries can be analysed.

Finally, the flux map on the receiver surface, calculated for a mesh of equally spaced nodes, is used to solve the mass flow rates of the molten salts and the surface temperatures through the local energy balances in each cell. A heat-transfer model of the receiver tubular walls (Singer et al., 2010; Boerema et al., 2013; Rodriguez-Sanchez et al., 2014; Sanchez-Gonzalez et al., 2017; Flesch et al., 2017) and some salt inlet and outlet temperatures are also necessary conditions to solve the heat problem.

As Falcone (1986) pointed out, correct sizing of the receiver requires checking a flux limit, which is closely related to the aiming strategy. Theoretically, all the heliostats in the field should be pointed to the cylinder equator to minimise receiver spillage, which is the fraction of the reflected rays out of the receiver surface. However, this would cause excessive energy concentration on the receiver surface and incident flux would reach peak levels above $2 \, MW/m^2$ (Relloso and Garcia, 2015). The solution is to re-aim some heliostats away from the receiver centreline to spread the flux distribution along the receiver and thus reduce peak flux below a limit value. The problem is that we do not know the details of the receiver design in its first stages, and strictly determining the flux limit requires a finite element analysis of creep and fatigue effects on receiver tubes in a specific thermal/hydraulic design (Falcone, 1986). In short, we have a circular problem, i.e. we cannot size the receiver because we do not have an allowed peak flux value, but we cannot calculate the peak flux because we do not have a specific receiver design. Obviously, the solution is to assume an approximate peak flux value to analyse re-aiming strategies and correctly size the receiver. After solving the thermal problem, the peak flux can be updated, if necessary.

Although the peak allowable incident flux is a function of the receiver working fluid and tube material and thickness, it is also strongly dependent on the scheduled lifetime and the number of receiver thermal cycles along it (Falcone, 1986). Falcone (1986) recommends a peak allowable incident flux of $0.85 \, MW/m^2$ for molten salt in fabricated receivers using 316 stainless steel, although the allowed peak flux for 9Cr1Mo tubes is clearly higher. DELSOL3 (Kistler, 1986) establishes that the default maximum allowable incident flux value in optimisation with receiver flux constraint is $1 \, MW/m^2$. Finally, Sener (Relloso and Garcia, 2015) comments that maximum peak allowed by the materials currently used for molten salts receivers is in the range $1–1.2 \, MW/m^2$.

Besides peak heat flux limited by creep and fatigue effects throughout the lifetime of the thermal cycles, the receiver must comply with some other limitations to operate reliably and safely. The two main constraints are corrosion of metal tubes in the presence of high film temperature of the molten salt, and excessive thermal stress in the tube walls (Vant-Hull, 2002; Sanchez-Gonzalez et al., 2017); both are also fulfilled through aiming strategies. Since the output parameter controlled by any aiming strategy is the flux distribution on the receiver, rather than film temperature or thermal gradient in the tubes, Vant-Hull (2002) suggested that both limitations were translated into a maximum allowable flux density (AFD) profile. Some examples of how various aiming strategies may achieve these AFD limits can be found in (Sanchez-Gonzalez et al., 2017; Flesch et al., 2017). The searching algorithms of the best AFD aiming strategies need to evaluate the actual flux map many times, so the map obviously changes due to aiming strategy variations.

The present work focuses on the second step of the complex receiver thermal design above-described and proposes a fast and reliable calculation of the flux map on the cylindrical receiver surface caused by a commercial-scale heliostat field. This important step, which connects both heliostat field and receiver designs, is considered the current bottleneck of receiver design.

Boerema et al. (2013) centre their work on assessing the surface temperatures for four different billboard ($1.50 \, m \times 1.50 \, m$) designs to develop a specific heat-transfer model. Given the billboard dimensions, a full treatment of the field (heliostat by heliostat) is avoided, and the actual field flux distribution on the receiver is approximated by a normal (Gaussian) distribution, with a mean located at the centre of the receiver. Astolfi et al. (2017), analysing some new aiming strategies using a Gemasolar-like plant as a case study, directly assume a Gaussian approximation for the heat-flux intensity along the receiver vertical line, which is fitted with a ray-tracing tool (SolTrace) and the analytic flux function produced by DELSOL. Astolfi et al. (2017) justify this approximation because optimising heat flux onto the receiver through aiming strategies generally needs a large number of iterations. Sanchez-

Gonzalez and Santana (2015) performed the full projection of 4550 heliostat flux images on the receiver panels of a Gemasolar-like plant. However, they report that the entire simulation of the overall distribution of flux on the receiver takes around 1 h of CPU time in an Intel Core i5-2400 microprocessor at 3.10 GHz with 4 GB of RAM memory. They use the UNIZAR model, which is an analytic expression for the flux density on the image plane based on the error function. Flesch et al. (2017) calculate the flux distribution on the receiver using the STRAL model, which is a ray-tracing tool developed at the German Aerospace Centre (DLR). Since the drawback of a large computational effort is recognised, a pre-calculation step is needed, in which the image of each heliostat is calculated and stored for each aim point before optimising the strategy.

With thousands of heliostats in commercial fields, the need for fast performance of the complete flux map on the receiver is rather high, not only for the above-commented AFD aiming strategies, but also for basic receiver sizing. All the above-mentioned studies on detailed receiver heat-transfer models and aiming strategies start with a given receiver diameter and height that are usually extracted from the scarce information on commercial plants.

As we have pointed out above, collector field optimisation supplies the receiver diameter (RD) and a preliminary receiver height (RH). The RH is not varied directly, but instead is approximated by a constant excess of RD so that high peak flux may be avoided later through aiming strategies without excessively increasing the spillage. Therefore, this preliminary RH should be checked later for the above-commented peak flux limitation, which basically requires a receiver flux map calculation.

It will be shown that the coherence of the overall flux map is supported by a differential energy balance, i.e. the power contained in a differential of area in the image plane has to be equal to the power contained in the projected differential of area onto the cylindrical receiver surface. Furthermore, this suggested coherence criterion could help to define the appropriate number of cells on the receiver surface. As far as the authors are aware, this verification has not been checked yet.

In conclusion, we present here a fast and reliable model for the flux map on a cylindrical receiver caused by a commercial-scale heliostat field. This model is based on the HFLCAL analytic function (Schwarzbölz et al., 2009) for the energy image sent by a heliostat on its image plane and on the projection, following the central reflected ray, of any point in the image plane onto the receiver surface. As an example of applying this new flux map model, the basic receiver sizing for a Noor III-like solar power tower plant (Relloso and Gutierrez, 2016) of 150 MWe and 7400 heliostats is analysed. Since a preliminary collector optimisation of this plant has already been presented elsewhere (Collado and Guallar, 2017a,b), only some necessary modifications are included here. Finally, the maximum peak flux has been checked to modify the preliminary receiver height, if necessary, found in the collector field optimisation.

2. Flux map on a cylindrical receiver caused by a heliostat field

The basic tool of the suggested procedure is the analytic flux density function of the energy reflected by a heliostat, usually defined on the plane normal to the central reflected ray and centred on the target point. This plane is called the image plane. The power sent by a heliostat P_h and contained on this image plane is (Collado, 2010)

$$P_h = DNI \cdot A_m \cdot \rho \cdot \cos\omega \cdot f_{sb} \cdot f_{at}, \tag{1}$$

where DNI is the instantaneous direct normal solar irradiance in (W/m^2), A_m the total mirror area (m^2), ρ the effective mirror reflectivity, i.e. the nominal one multiplied by a cleanliness factor, and $\cos\omega$ the cosine of the incidence angle between the sun's rays and the heliostat normal. f_{sb} is the shadowing (of incident sunlight by neighbour heliostats) and blocking (of reflected sunlight by adjacent mirrors) factor, i.e. the

fraction of the heliostat area free from shadowing and blocking, and, finally, f_{at} is the atmospheric attenuation factor. Here we use the HFLCAL model for the attenuation factor (Schmitz et al., 2006); the f_{sb} calculation has been already explained in detail elsewhere (Collado and Guallar, 2013).

2.1. HFLCAL flux density model on image plane

The HFCAL flux density model (Schwarzbölz et al., 2009), developed at the German Aerospace Centre (DLR), is a circular normal distribution that assumes all heliostats have well-canted concentrating facets of spherical curvature. Its mathematical expression on the image plane is

$$F_{image}(x,y) = \frac{P_h}{2\pi\sigma_{HF}^2}\exp\left(-\frac{(x^2+y^2)}{2\sigma_{HF}^2}\right) \quad (2)$$

where P_h is the power sent by the heliostat, see Eq. (1), and the effective deviation σ_{HF} is the convolution of the four Gaussian error functions considered: the sun-shape error, here $\sigma_{sun} = 2.51 \cdot 10^{-3}$ rad; beam quality σ_{bq}; the astigmatic effect σ_{ast}, which is related to the image dimensions of the heliostat reflected onto the image plane; and, finally, the tracking error σ_t, which accounts for the deviation of the central reflected ray from the aim point. Then σ_{HF} is

$$\sigma_{HF} = \sqrt{D^2(\sigma_{sun}^2 + \sigma_{bq}^2 + \sigma_{ast}^2 + \sigma_t^2)}, \quad (3)$$

where D is the actual distance from the heliostat centre to the actual aim point. The beam quality σ_{bq} accounts for the deviations of the mirror curvature from the ideal shape and imperfections of the reflecting surface due to waviness and roughness; it is related to the slope error σ_s, measured from the heliostat normal, namely, $\sigma_{bq}^2 = (2\sigma_s)^2$. Finally, the tracking error σ_t is measured from the central reflected ray (Collado, 2010), whereas the expression of the astigmatic effect σ_{ast} considers the incidence cosine and some image dimensions in the tangential and sagittal planes (see Schwarzbölz et al., 2009).

2.2. Intercept factor and aim point

The intercept factor is the fraction of the total power sent by a heliostat that actually hits the cylindrical receiver, i.e. it is equal to one minus the spillage. Its mathematical expression would be the integration of the flux function on the image plane where the bounds are defined by the projection of the cylinder contours onto the image plane in the direction of the central reflected ray **t** of the heliostat, see Fig. 1. This unitary vector **t** depends on the heliostat's location and actual aim point.

This aim point, on the cylinder surface, usually has the same azimuth as the heliostat. However, its height (zR), with origin in the equator, is the result of an aiming strategy to spread the energy spots along the receiver height. If zR were equal to zero (heliostat aiming at the equator), the intercept would be maximum. However, as we have already commented, if all the mirrors were pointed at the same height, the peak flux could sometimes be excessively high.

Therefore, the intercept factor as the integration of the unit flux density function, with the projected contours of the cylinder onto the image plane as bounds, is, see Fig. 1,

$$f_{int} = \int_{x=-RR}^{x=RR} \frac{1}{\sigma_{HF}\sqrt{2\pi}}\exp\left(-\frac{x^2}{2\sigma_{HF}^2}\right)dx \cdot \int_{y=\left(-\frac{RH}{2}-zR\right)\cos\gamma}^{y=\left(\frac{RH}{2}-zR\right)\cos\gamma} \frac{1}{\sigma_{HF}\sqrt{2\pi}}\exp\left(-\frac{y^2}{2\sigma_{HF}^2}\right)dy, \quad (4)$$

where RR is merely the radius of the receiver and cos γ is the incidence cosine of the central reflected ray on the cylindrical surface, see Fig. 1. The integration of these exponential functions is immediate through the error function

$$f_{int} = erf\left(\frac{RR}{\sigma_{HF}\sqrt{2}}\right)\frac{1}{2}\left(erf\left(\frac{\left(\frac{RH}{2}-zR\right)\cos\gamma}{\sigma_{HF}\sqrt{2}}\right) - erf\left(\frac{\left(-\frac{RH}{2}-zR\right)\cos\gamma}{\sigma_{HF}\sqrt{2}}\right)\right). \quad (5)$$

2.3. Instantaneous optical efficiency of the heliostat

Finally, the instantaneous optical efficiency of a heliostat η_{opt} would be defined as the fraction of the maximum power sent by the heliostat, $DNI \cdot A_m$, that actually reaches the receiver

$$\eta_{opt} = \rho \cdot \cos\omega \cdot f_{sb} \cdot f_{at} \cdot f_{int}. \quad (6)$$

2.4. Flux density on the cylinder surface

We define a very simple coordinate system to locate any point on the cylinder surface, see Fig. 1. x_c is a circumference arc with a north origin, positive counter clockwise, and equivalent to the azimuth θ of that point. θ has a south origin and positive clockwise in the same way as the heliostat azimuth α_T. h is a vertical coordinate on the cylinder surface with origin at the equator and positive upwards.

Following the central reflected ray **t**, the projection of some points (x, y) in the image plane onto the cylinder surface will be point (x_c, h). The relation between them is immediate from Fig. 1
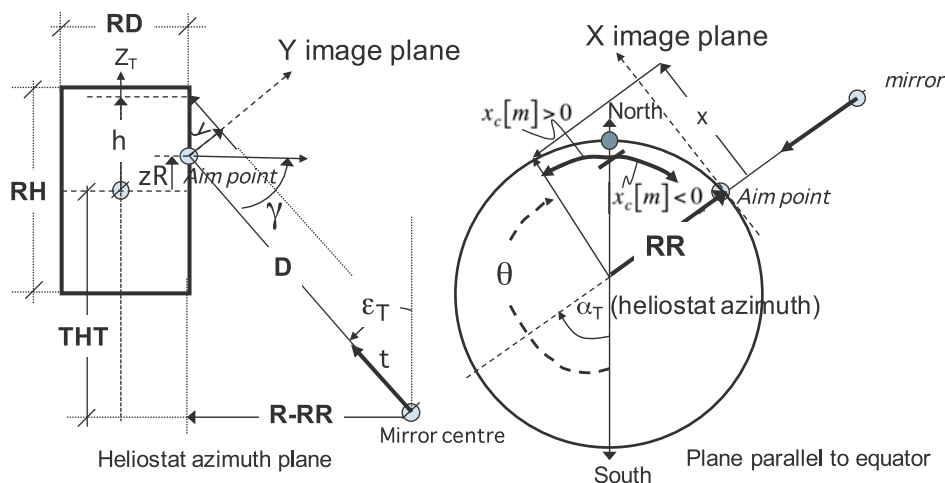

Fig. 1. Projection of a point (x, y) in the image plane into a point (x_c(θ), h) on the cylindrical surface.

Table 1
Parameters used in the optimisation of Noor III-like collector field.

Dimension	Values used in the optimisation	Noor III data (Relloso and Gutierrez, 2016)
DNI [kWh/m^2/year]	2268 (Meinecke, 1982) PSA-Almería	2500
Annual sunlight hours N_{hours}	2790 (Meinecke, 1982) PSA-Almería	
Solar field area	550 Ha	550 Ha
Number of heliostats	7400	7400
Heliostat height HH	12.30 m (assumed)	
Heliostat width HW	15.36 m (assumed)	
Heliostat mirror area Am	178.5 m^2	178.5 m^2 (HE54)
Heliost. Diagonal DH	19.67 m (assumed)	
Tower optical height THT	250 m	250 m
Number of heliostats in the first row	60 (Collado and Guallar, 2017a)	
Receiver thermal (absorbed) power	660 MWth	660 MWth
Rec. Diameter RD	[14, 16, 18, 20, 22] m (assumed)	
Receiver height RH	1.2 × [14, 16, 18, 20, 22] m (assumed)	
Nominal electric power	150 MWe	150 MWe
Thermal storage hours	7.5	7.5
Non-dimensional layout settings	$\Delta r_1 = 0.866$ $\Delta r_2 = [0.866, 1.0]$ $\Delta r_3 = [1.6, 1.8, 2.0]$	
Standard dev. slope surface error	1.53 mrad (SAM-NREL, 2018)	
Standard dev. tracking error	1.53 mrad (assumed)	
Standard dev. sunshape	2.51 mrad (Collado and Guallar, 2013)	
Nominal reflectivity × cleanliness	0.9 × 0.99 (SAM-NREL, 2018)	
Attenuation model	HFLCAL (Schmitz et al., 2006)	

$$h = zR + \frac{y}{\sin \varepsilon_T} \Rightarrow y = (h - zR)\sin \varepsilon_T$$

$$\theta = \alpha_T + \arcsin\left(\frac{x}{RR}\right); \quad x_c = RR(\pi - \theta) \Rightarrow x = RR \cdot \sin(\theta - \alpha_T) \tag{7}$$

Then, the flux density on the cylinder is derived from a differential energy balance. Consequently, the energy contained in a differential surface of the image plane centred on (x, y) should be equal to the energy contained in a differential surface of the cylinder centred on its corresponding projected point (x_c, h)

$$F_{cylinder}(x_c,h)dx_c dh = F_{image}(x,y)dxdy \Rightarrow F_{cylinder}(x_c,h)$$
$$= F_{image}(x,y)\left\|\frac{dxdy}{dx_c dh}\right\| \tag{8}$$

The factor of the flux image in Eq. (8) is called the Jacobian of the transformation and its meaning is merely an area ratio, which has no sign; thus, there is a double vertical bar, one for the determinant and the other for the absolute value. This determinant can be easily derived from the transformation defined by Eq. (7)

$$Jacobian = \left\|\frac{dxdy}{dx_c dh}\right\| = \left\| \begin{array}{cc} \frac{\partial x}{\partial \theta}\frac{\partial \theta}{\partial x_c} & \frac{\partial x}{\partial h} \\ \frac{\partial y}{\partial x_c} & \frac{\partial y}{\partial h} \end{array} \right\| = \left\| \begin{array}{cc} -\cos(\theta - \alpha_T) & 0 \\ 0 & \sin \varepsilon_T \end{array} \right\|$$
$$= |\sin \varepsilon_T \cos(\theta - \alpha_T)|. \tag{9}$$

Therefore, the flux density function on the cylinder surface is

$$F_{cylinder}(x_c,h) = F_{image}(x,y)|\sin \varepsilon_T \cos(\theta - \alpha_T)| \tag{10}$$

Finally, to highlight that the total power obtained from the integration of the two terms of the differential energy balance, Eq. (8), over corresponding domains should be the same

$$\int_{cylinder} F_{cylinder}(x_c,h)dx_c dh = \int_{cylind.\ onto\ image\ plane} F_{image}(x,y)dxdy. \tag{11}$$

$$\int_{cylinder} F_{cylinder}(x_c,h)dx_c dh = \sum_{x_c}\sum_{h} F_{cylinder}(x_c,h)\Delta x_c \Delta h$$
$$= DNI \cdot A_m \cdot \eta_{opt-numeric}. \tag{12}$$

$$\int_{cylind.\ onto\ image\ plane} F_{image}(x,y)dxdy = DNI \cdot A_m \cdot \eta_{opt-analytic}, \tag{13}$$

where $\eta_{opt-analytic}$ is defined by Eq. (6), in which the above analytical integration is already solved and included in the intercept factor, see Eqs. (4) and (5). Furthermore, the numerical integration of the flux function on the cylinder yields all the incident power, Eq. (12), which, divided by the maximum theoretical power, gives $\eta_{opt-numeric}$. Therefore, both efficiencies have to be equal. This coherence criterion may help to select the appropriate number of cells over the cylinder surface.

The suggested procedure for every heliostat in the field, which is partially based on the work by Sanchez-Gonzalez and Santana (2015), consists of four steps:

(1) The cylindrical surface is discretised in a mesh of equally spaced nodes of coordinates ($x_c(\theta)$, h).
(2) The Jacobian is calculated for each node, Eq. (9). If the node is out of the zone of the cylinder that can be seen from the heliostat, the Jacobian is set to zero.
(3) Mesh nodes are projected onto the image plane in the direction of **t**, Eq. (7), obtaining (x, y).
(4) The flux density function on the image plane is now evaluated in (x, y), Eq. (2), and multiplied by the Jacobian, Eq. (9), thus finally yielding the flux density on the cylinder caused by the heliostat.

3. Optimised design of the collector field for Noor III-like

3.1. Parameters used for the optimisation

Recently, Sener (Relloso and Gutierrez, 2016) has provided some design details about the Noor III project, which is under construction in Morocco. The Noor III 150 MWe project, with 7400 heliostats (radially staggered surrounding field) and 7.5 h of molten-salt storage, will be the case study of this work. Table 1 shows the main parameters used in the optimised design of the collector field of a Noor III-like plant outlined in this work. Remember that the optimisation supplies the receiver diameter RD and a preliminary receiver height RH.

The authors have already recently explored the optimised design of this collector field using the campo code (Collado and Guallar, 2017a,b). However, although the TMY used was that of PSA Almería (Meinecke, 1982), the annual DNI included was that of Noor III, i.e. 2500 kW h/m^2/year. Besides, the standard deviation of tracking error chosen was $\sigma_t = 0.63 * 10^{-3}$ rad, currently considered to be low because these data are based on the tracking tests (Lata et al., 2010) of Sener heliostat HE35 (Gemasolar) with an area of 115.7 m^2, which is much smaller than that of the Sener HE54 model used in Noor III, see Table 1. This previous optimisation followed the same procedure used by Collado and Guallar (2016), i.e. first searching the best layouts for every set of design variables (THT, RR) and then calculating the LCOE based on the receiver radius (RR) for the checked tower heights. The THT proven were [200, 225, 250, 275] m. It was found (Collado and Guallar, 2017b) that the optimum tower optical height THT was 250 m.

This tower height agrees with Sener data (Relloso and Gutierrez, 2016); consequently, in this work, THT is fixed at 250 m, see Table 1. Based on previous analyses (Collado and Guallar, 2017b), the checked RR interval here is [7, 8, 9, 10, 11] m, equivalent to the receiver diameter (RD) interval in Table 1, whereas the RH is assumed to be 20% higher than the corresponding RD.

According to Collado and Guallar (2016), searching for a layout for 7400 heliostats with a higher field efficiency η_{field} is merely equivalent

to finding two non-dimensional settings Δr_2 and Δr_3, and the number of heliostats in the first row in the first zone $Nhel_1$. The former define the constant radial increment between consecutive rows in zones 2 and 3 of the field, i.e. $\Delta r_2 * DM$ and $\Delta r_3 * DM$, respectively, where DM is the heliostat diagonal, see Table 1. For the first zone, the closest to the tower, Δr_1 is always set to 0.866, which is the minimum possible value due to mechanical limits. Concerning $Nhel_1$, Collado and Guallar (2017a) have already analysed that the most efficient value for THT = 250 m was $Nhel_1 = 60$, which is equivalent to a radius in the first row of around $0.75*THT$, as DELSOL recommends. Finally, the number of rows for each field zone is defined for the densest field and they are not varied along the optimisation (Collado and Guallar, 2013).

3.2. Optimum layouts, LCOE calculation and receiver sizing

By running campo code (Collado and Guallar, 2016) with the parameters in Table 1, and with all the heliostats pointing to the receiver equator, i.e. minimum spillage, the best field efficiency η_{field} for each receiver radius tested and the corresponding optimum layouts have been found. The optimum Δr_2, for any receiver radius, is 0.866, the minimum value, whereas $\Delta r_3 = 1.6$ and $\Delta r_3 = 1.8$ give the best field efficiencies for RR = [7, 8] and RR = [9, 10, 11], respectively. A constant radial increment could be thought to result in a lot of blocking in the outer part of the zone and even to make increasing the radial spacing with radius necessary. However, in line with preliminary findings presented in Collado and Guallar (2017b), denser fields, with constant radial increments, yield higher field efficiencies for very large fields. The huge dimensions of the field, which extends up to 2 km from the tower to the North, while the distance from East to West might be almost 4 km, could justify these results. Since the distances between the outer zone mirrors and the receiver are very long in such a field, besides the blocking, both the spillage and the attenuation, which are sensitive to long distances, will be very significant in the outer zone and could lead to denser fields.

The LCOE equation used here is based on Kolb (2011) and SAM-NREL (2018), namely

$$LCOE\,[\text{¢/kWh}_e] = \frac{\frac{i(1+i)^{N_Y}}{(1+i)^{N_Y}-1}C_{plant} + AnnualOM}{E_E * Availability}$$
$$= \frac{FCR*C_{plant} + AnnualOM}{E_E * Availability} \tag{14}$$

where the fixed charge rate (FCR) is a single parameter (Kolb, 2011) representing all the capital-financing-related assumptions in the analysis. Here the value used is the same as Kolb (2011), i.e. FCR = 0.075, which would be equivalent to a yearly nominal interest of the loan i = 6.5% for $N_Y = 30$ years. Also, following Kolb (2011), plant availability is 90%. The details of the installed capital costs C_{plant} and the operation and maintenance annual costs (OM), both mainly based on (NREL-SAM, 2018), are shown in Table 2.

In Table 2, the SAM tower cost model is based on the actual tower height; therefore, half the receiver height (RH) is subtracted from the tower optical height (THT = 250 m) and then half the heliostat height (HH), see Table 1, as an approximation of the heliostat pedestal height, is added.

The net annual energy output $E_E(\text{kWh}_e)$, in the denominator of Eq. (14), is calculated for the five receiver designs in Table 1 following the DELSOL system optimisation as outlined by Collado and Guallar (2016). Therefore, only the main details are explained.

The core of this annual energy is the field efficiency η_{field} found for the corresponding receiver radius and optimised layout. First, the annual gross receiver energy, or annual incident energy onto the receiver, is calculated

$$E_{inc} = A_m N_{hel} DNI \eta_{field} \tag{15}$$

where A_m is the mirror area of an individual heliostat, N_{hel} is the number of heliostats in the field and DNI is the annual direct normal insolation based on data for PSA Almería, see Table 1.

For the sake of convenience, in Table 2, we choose RR = 8.5 m, RH = $1.2 * RD = 20.4$ m and THT = 250 m as a reference case, in which, as we will see later, $\eta_{field} = 56.58\%$. Thus, from Eq. (15), $E_{inc} = 178.5 \cdot 7400 \cdot 2268 \cdot 0.5658 \cdot 10^{-6} = 1695.02$ GWh. This value of E_{inc} is used to subtract annual receiver losses $L_{thermal}$ (receiver radiation and convection losses). The annual energy the molten salts absorb at the receiver E_{abs} is

Table 2
Cost models for LCOE. Noor III 150 MWe. Reference case (RR = 8.5 m, RH = 1.2 * RD = 20.4 m, THT = 250 m).

	Cost (NREL-SAM 2018)	Noor-III (Sener, 2017)	Capital cost ($M)
Direct capital cost (installed)			
Site improvement	$16/m²-mirror	(7400 × 178.5) m²-mirror	21.13
Heliostat field	$130/m² (SolarPACES, 2017)	(7400 × 178.5) m²-mirror	171.72
Tower	$3 \cdot e^{0.0113*HT}$	$HT = 250 - RH/2 + HH/2$	48.32
Receiver	$103 \cdot (AR/1571)^{0.7}$	$AR = 1089.5$ m²	79.72
Thermal storage (7.5 h.)	$24/kWh$_t$	$E_t = 7.5 \cdot (150{,}000/\epsilon_{cyc})$	65.53
Power cycle + Balance of plant	$1440/kW$_e$	150,000 kW$_e$	216
Subtotal			602.4
Contingency	7% of subtotal		42.17
Total direct capital cost			**644.57**
Indirect capital cost			
Land	$2/m²-land	5.5 * 10⁶ m²	11.00
EPC + Owner cost	13% direct cost	0.13 × 644.57	83.79
Sales tax	5% of (80% direct cost)	0.05 × 0.8 × 644.57	25.78
Total indirect costs			**120.57**
CAPITAL COSTS	Total direct + total indirect		**765.14**
Annual O & M costs			
Fixed cost by capacity	$66/kW-yr (net output)	66 × 135,000 ($\epsilon_{aux} = 0.9$)	8.91
Variable cost by generation	$3/MWhe	3 × 554584.0	1.66
ANNUAL O & M COSTS			**10.57**

E_E (GWh$_e$) = **554.584 GWh$_e$**; $LCOE\left(\frac{cents}{kWhe}\right) = \frac{FCR \cdot Capit.\,costs + OM}{E_E \cdot Plant\,Availability} = \frac{(0.075 \cdot 765.14 + 10.57)10^2}{554.584 \cdot 0.9} = 13.61.$

$$E_{abs} = \alpha_s \cdot E_{inc} - L_{thermal}, \tag{16}$$

where $\alpha_s = 0.94$ is the assumed receiver solar absorptance of the tube panels (Collado and Guallar, 2016).

As a first approximation, the hourly and seasonal variation of thermal losses and the average wall temperature T_{wall} were assumed to be negligible. The value of T_{wall} used here, 763 K, was calculated by Collado and Guallar (2016) assuming a maximum wall temperature at the outlet receiver of 900 K. Therefore, the expression of the annual thermal losses, in which the individual losses for radiation, and forced and natural convection are calculated separately and summed, is

$$L_{thermal} = (Q_{rad} + Q_{conv})N_{hours} = [\varepsilon \sigma A_R (T_{wall}^4 - T_{amb}^4) + h_{mix} A_R (T_{wall}$$
$$-T_{amb})]N_{hours} \tag{17}$$

where $\varepsilon = 0.9$ is the total hemispherical emittance (Collado and Guallar, 2016) and σ is the Stefan-Boltzmann constant (5.67×10^{-8} W/m^2 K^4). $A_R (=2\pi RR \cdot HR)$ is the lateral surface of the cylindrical receiver (m^2), which is also used in the receiver cost model in Table 2. T_{amb} is the ambient air temperature (here assumed to be about 293 K), h_{mix} a mixed convection coefficient, which is a combination of forced and natural convection mechanisms, and based on Collado and Guallar (2016), a value of $h_{mix} = 16.61$ (W/m^2 K) is chosen. Finally, N_{hours} are the real sunshine hours of the TMY used in this paper, 2790 h for Almería using meteorological GAST data (Meinecke, 1982).

Then, for the reference collector field, $A_R = 1089.5$ m^2 and the annual thermal losses are $L_{thermal} = 75.16$ GWh$_t$ so, from Eq. (16), the annual absorbed energy on the receiver is $E_{abs} = 1518.16$ GWh$_t$.

Now, to arrive at the net annual electric output E_E, E_{abs} is multiplied by a set of constant annual averaged efficiency factors ϵ_i, which are assumed to be time independent (Kistler, 1986),

$$E_E = \epsilon_{pip} \epsilon_{sto} \epsilon_{aux} \epsilon_{cyc} \, E_{abs} \tag{18}$$

where ϵ_{pip} is the piping insulation losses efficiency, ϵ_{sto} is the thermal storage efficiency, ϵ_{aux} is the auxiliary loads efficiency, and, finally, ϵ_{cyc} is the cycle thermal efficiency. For the first three efficiency factors, we take the same values mentioned by Collado and Guallar (2016) namely, $\epsilon_{pip} = 0.99$, $\epsilon_{sto} = 0.995$ and $\epsilon_{aux} = 0.9$. Note that ϵ_{aux} is the net output power to gross power ratio, see Table 2. Concerning the thermodynamic efficiency of the power cycle, we have taken $\epsilon_{cyc} = 0.412$ (NREL-SAM, 2018), which is also used in Table 2 to calculate the thermal energy stored. For the reference case in Table 2, the net annual electric output results in $E_E = 554.58$ GWh$_e$, which is used to calculate the LCOE of the reference case at the end of Table 2.

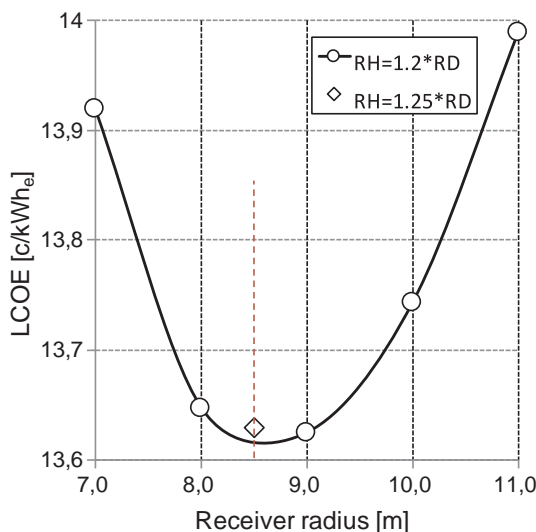Finally, Fig. 2 shows the LCOE profile, Eq. (12), based on the

receiver radius (RR) for THT = 250 m. Remember that the receiver height has been assumed equal to 1.20∗RD. A receiver radius of RR = 8.5 m (RD = 17 m, RH = 20.4 m) has the minimum LCOE value. This is the primary sizing of the cylindrical receiver. In (Collado and Guallar, 2017b), given the LCOE scale and the short vertical distances between the LCOE profiles for THT equal to 225, 250 and 275 m, note that the number of survey points to draw the LCOE profile seems suitable.

4. Verification of the allowable peak flux for the optimised design of the collector field

The annual optical efficiency of a single heliostat is the annual average along the Almería TMY of its instantaneous optical efficiency, Eq. (6). Fig. 3 shows the annual efficiency map for a collector field with 7400 Sener HE54 heliostats, with THT = 250 m, and a cylindrical receiver with dimensions RR = 8.5 m and RH = 20.4 m. It has been checked that its optimum layout is Nhel₁ = 60, $\Delta r_1 = 0.866$, $\Delta r_2 = 0.866$ and $\Delta r_3 = 1.6$. As we have commented above, its field efficiency $\eta_{field} = 56.58\%$, which is the average of the individual values over the whole field. In this map, the trimming boundary of the heliostat field is already defined. Remember that campo starts efficiency calculations with several heliostats in excess of the nominal (10,000) and then the 7400 heliostats with the highest efficiency are selected.

We next check the peak flux caused by this collector field onto the receiver at the worst time of the year, i.e. summer solstice noon (day 172, solar hour 12), using the flux density function on the cylinder surface detailed in Section 2. Previously, an aiming strategy has to be chosen to define the height of the aim point (zR) for every heliostat in the field.

4.1. Multi-aiming strategy

To avoid probable excessive peak fluxes, we follow the multi-aiming strategy implemented by Sanchez-Gonzalez and Santana (2015), which adjusts each heliostat target position along the vertical direction on the surface of the cylindrical receiver, see Fig. 1. This aiming strategy is based on the suggestion of Vant-Hull (2002) that the position of the aim point could be estimated from the radius of the reflected beam. The mirror is then aimed at the receiver in such a way that the beam circumference is tangent to either the upper or the lower receiver edge. As
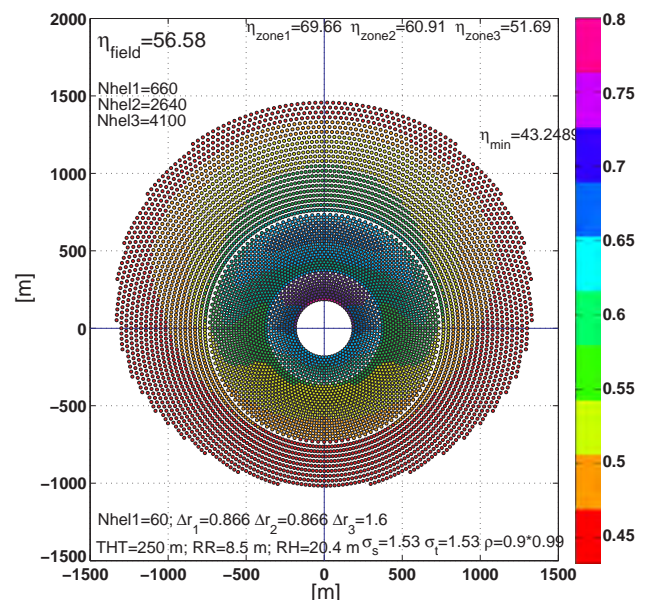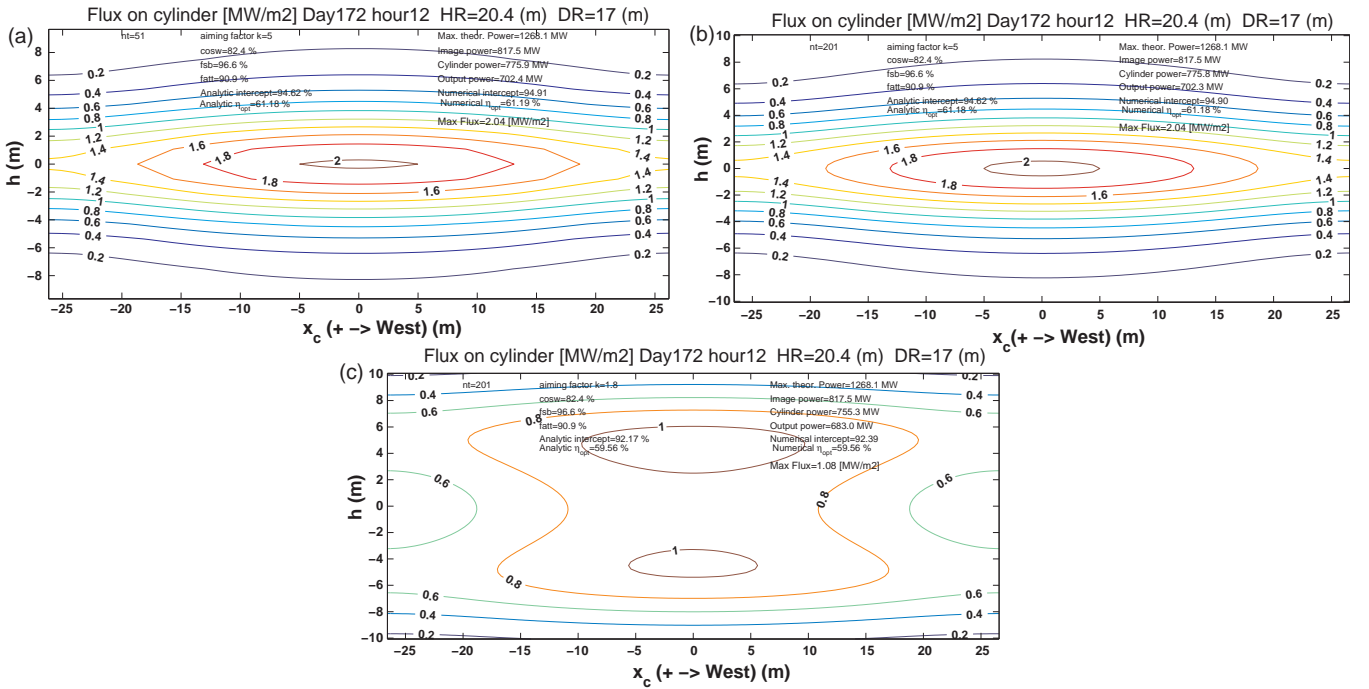

Fig. 2. LCOE profile vs receiver radius for THT = 250 m and RH = 1.2 × RD.

Fig. 3. Map of the annual optical efficiency for a Noor III-like plant with RR = 8.5 m and RH = 20.4 m.

Fig. 4. Flux map (MW/m^2) on the unfolded cylindrical receiver RR = 8.5 m, RH = 1.2 × RD. (a) Aiming factor k = 5 and number of azimuth cells nt = 51. (b) Aiming factor k = 5 and number of azimuth cells nt = 201. (c) Aiming factor k = 1.8 and number of azimuth cells nt = 201.

full details of this aiming strategy can be found in Sanchez-Gonzalez and Santana (2015), only the relevant equations used in this work are commented on briefly.

The target point is located from the upper or the lower edge, in alternate heliostat rows, at a distance equal to the projection of the beam radius. This beam radius depends directly on the adopted error angle $\frac{k\sigma_{HF}}{D}$, see Eq. (3), where k is defined as an aiming factor that typically ranges between 0 and 3. For a normal distribution, 99.7% of the reflected flux is within the beam subtended under $\frac{3\sigma_{HF}}{D}$. Since the error angle $\frac{k\sigma_{HF}}{D}$ is small, the radius of the reflected beam at the image plane can be estimated as $k\sigma_{HF}$, and its projection into the receiver vertical is

$$rk = \frac{k\sigma_{HF}}{\sin\varepsilon_T},$$ (19)

where ε_T is the elevation angle, from the zenith, of the central reflected ray of the heliostat, see Fig. 1.

In this work, the target point (zR), see Section 2, is located from the equator instead of from the receiver edges. The aiming procedure for any row begins checking if the projection of the beam diameter 2rk is greater than the receiver height, i.e. RH < = 2rk, then the heliostat would be aimed at the receiver equator (zR = 0.0). Otherwise, for odd rows (upwards equator)

$$zR = \frac{RH}{2} - rk,$$ (20)

whereas for even rows (downwards equator)

$$zR = -\frac{RH}{2} + rk.$$ (21)

With k = 5, the flux pattern is equal to that with equatorial aiming. However, as we reduce the aiming index k, the flux distribution would flatten along the equator belt due to the spread of hot spots along the receiver vertical.

4.2. Flux map on a cylindrical receiver with RR = 8.5 m and HR = 20.4 m for a different number of cells and aiming factors

The cylindrical surface has to be discretised in a mesh of equally

spaced nodes of coordinates ($x_c(\theta)$, h).

The number of cells along the azimuth coordinate θ is nt, which is also the number of columns in the matrix that represents the unfolded cylindrical surface. The width, in metres, of the cell is

$$dimcellt_. = \frac{2\pi RR}{nt}.$$ (22)

Now, the number of cells (nh) for the h coordinate, along the vertical of the cylinder, is calculated with the condition that the height of the cell is practically equal to its width

$$nh = round\left(\frac{HR}{dimcellt}\right),$$ (23)

where the quotient is rounded off to the next lowest integer because nh is an integer.

Fig. 4a shows the flux map on the unfolded cylindrical receiver with RR = 8.5 m and HR = 1.2*RD (20.4 m). The aiming factor k is equal to 5.0, which is equivalent to all heliostats pointing to the equator. The number of cells along θ is nt = 51, so the number of cells along h is nh = 61, i.e. a total of nt x nh = 3111 cells. The simulation of the flux map on the receiver takes around 6 s of CPU time in a quad-core Intel Core i5 at 2.66 GHz with 8 GB of RAM.

The coherence criterion for the practical equality of the analytic optical efficiency and the numeric one, see Eqs. (11)–(13), is verified, which would confirm the nt value chosen. However, the flux contours are not smooth enough with peaks on the contours' horizontal extremes.

Fig. 4b shows the same map for the same aiming factor (k = 5.0) but now with nt = 201. The CPU time rises to 43 s, although the flux contours are now smooth. The peak flux is 2.04 MW/m^2, which is clearly higher than the maximum peak allowed by the tube materials, i.e. in the range 1–1.2 MW/m^2 (Relloso and Garcia, 2015). Given this allowable interval, a maximum flux < 1.1 MW/m^2 could be considered a conservative limit.

Fig. 4c, with k = 1.8, explores the decrease of the aiming factor to abate the peak flux produced. For k = 1.8, meaning a much greater spots dispersion than before, the peak flux lowers to 1.08 MW/m^2, which would be an appropriate value. However, due to the spillage
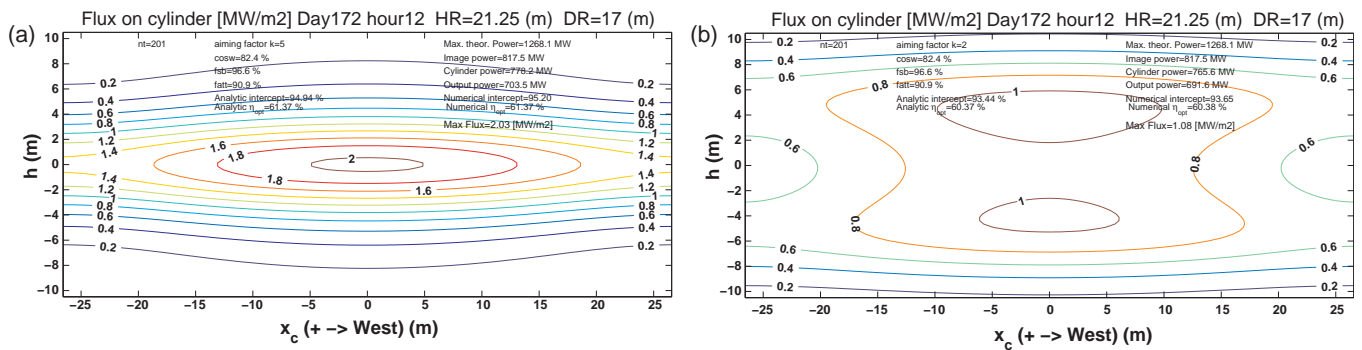
Fig. 5. Flux map (MW/m^2) on the unfolded cylindrical receiver RR = 8.5 m, RH = 1.25 × RD. (a) Aiming factor k = 5, nt = 201. (b) Aiming factor k = 2, nt = 201.

increase, the optical efficiency (59.56%) is reduced by 1.6 percentage points compared to the optical efficiency of the equator aiming (k = 5.0) (61.18%). The output power with an allowed peak flux, in spite of the increased spillage, is 683 MWth, greater than the design receiver thermal load, i.e. 660 MWth, and it fulfils the specifications without problems, see Table 1.

4.3. Flux map on a cylindrical receiver with RR = 8.5 m and HR = 21.25 m for different aiming factors

Finally, we analysed the effect of increasing the receiver height on the peak flux and the spillage. Now RH is set to 25% higher than the receiver diameter, i.e. RH = 1.25∗DH = 21.25 m. The receiver radius is the same as before, namely RR = 8.5 m. Besides, given the small variation in height, the field layout is considered the same as before.

Fig. 5a shows the contour flux for a greater receiver height and an aiming factor of k = 5.0. The peak flux (2.03 MW/m^2) is again excessive, although the optical efficiency grows slightly to 61.37% due to the rather moderate reduction in spillage (compare Fig. 5a with Fig. 4b). However, with k = 2.0, see Fig. 5b, the peak flux is lowered to 1.08 MW/m^2, which is an acceptable maximum value. The optical efficiency has decreased to 60.37%, around 1.0 percentage point less than that of the equator aiming (k = 5).

To compare both receivers with the same diameter but different heights, the LCOE of this second receiver with RH = 21.25 m has been calculated and included in Fig. 2. The higher receiver (RH = 1.25∗RD) has a slightly higher LCOE than that of RH = 1.2∗RD. The advantage of a taller receiver might not be so clear. However, field efficiency, used to evaluate the annual energy, thus the LCOE, is calculated with the simplest aiming strategy, i.e. all the heliostats pointing to the receiver equator. Therefore, strictly speaking, the annual field efficiency (and the LCOE) should be based on intercepts with peak fluxes lower than the allowable maximum flux.

5. Discussion and conclusions

This paper presents a new procedure to calculate the flux map caused by a heliostat field on external cylindrical receivers of solar power tower plants. It is based on the analytic HFLCAL model of flux density produced by a heliostat (a circular Gaussian) on its image plane and on the simple and coherent projection of any point in the image plane onto the cylindrical receiver surface following the central reflected ray.

The HFLCAL flux density for any heliostat includes effective reflectivity, cosine of the incidence angle, shadowing and blocking factor and atmospheric attenuation, which are calculated in the general framework of the campo code (Collado and Guallar, 2012, 2013). Campo can perform accurate analysis of the shadowing and blocking factor f_{sb} for every heliostat in the field. Note that Besarati and Goswami (2014) and Gadalla and Saghafifar (2016) have independently verified the Collado and Guallar (2012) f_{sb} results.

An analytic expression, based on the error function, of the intercept factor for a heliostat pointing to some point at a height (zR) from the equator (due to aiming strategies) is, as far as the authors are aware, presented for the first time.

The numeric calculation of the intercept, through the summation over the receiver, of the flux on cylindrical surface cells multiplied by the cell area, is coherent with the analytical intercept so the analytic optical efficiency of the field is equal to the numerical one. This is because the new function of the flux on the cylinder is derived from a differential energy balance, which connects it with the HFLCAL flux on the image plane and their respective differential areas.

The standard deviations of slope and tracking Gaussian errors used in the HFLCAL model to simulate the energy spot sent by Sener HE54 heliostats (Relloso and Garcia, 2015) are based on reasonable escalations of slope and tracking errors derived, by Lata et al. (2010), from actual data measured for much smaller heliostats, i.e. Sener HE35.

Consequently, the flux map calculation is considered a reliable model since the flux density model has been checked against measured energy spots (Collado, 2010) and it can fit them, through the slope error, with reasonable accuracy, but also because, as we have commented above, there is mathematical coherence between the analytic and the numerical integrations of the density flux model.

The whole simulation of the overall distribution of the flux caused by 7400 heliostats on the receiver surface, divided into 3111 cells, takes around 6 s of CPU time in a quad-core Intel Core i5 at 2.66 GHz with 8 GB of RAM memory. Thus, the presented flux map projection is much faster than the model proposed by Sanchez-Gonzalez and Santana (2015), which is the only published model to date that performs a full projection of 4550 heliostat flux images on the receiver surface, and it takes around 1 h of CPU time in an Intel Core i5 microprocessor at 3.10 GHz with 4 GB of RAM memory.

However, the simulation presented here is based on a perfect cylindrical surface, even though the actual receivers consist of flat panels (Sanchez-Gonzalez and Santana, 2015). Nevertheless, it should not be very difficult or time-consuming to project the cylinder flux into flat panels approximating a cylindrical surface.

An example of the basic sizing of a receiver for a Noor III-like plant with 7400 heliostats and a tower height of 250 m, using the campo code and the new cylinder flux function, is also presented. The sizing fulfils the maximum allowable flux using a multi-aiming strategy suggested by Vant-Hull (2002) and put into practice by Sanchez-Gonzalez and Santana (2015), but with the collateral effect of increasing the spillage.

However, flux maps could be made even flatter with less spillage (allowing for a shorter receiver) if more sophisticated level aim strategies were employed, such as those used at Solar One/Two (Vant-Hull, 2012) or the recent proposals made by Astolfi et al. (2017). Note also that the high temperature flux limit is not addressed. It would, therefore, be necessary to watch the aim points near the receiver outlet particularly if the energy spot shifts are applied to lower peak flux (Vant-Hull, 2012).

The effect of slightly increasing the receiver height from 20% to 25% higher than the diameter was also analysed. It is clear that the taller receiver collects more power than the shorter one, although the taller receiver's LCOE is slightly higher than that of the shorter one. This result may be logical because the higher the receiver height, the lower the peak flux and the spillage, but the higher the area, then the higher the receiver cost and the thermal losses.

However, in this work, the annual energy, therefore, the LCOE, is calculated with all the heliostats pointing to the receiver equator. Consequently, strictly speaking, the annual field efficiency (and the LCOE) should be based on intercepts with peak fluxes lower than the allowable maximum flux. It is clear, as Relloso and Garcia (2015) point out, that not considering receiver peak flux limitations in the simulation would lead to a non-realistic over prediction in annual performance.

Finally, it is worth noting that a fast and coherent flux map on the cylinder, as presented in this work, would be a valuable tool for basic receiver sizing, or calculating the annual field performance considering peak flux limitations. It would also be useful for searching for optimum strategies to fulfil the AFD profile, for exploring how to flatten the flux pattern onto the receiver, or for solving the receiver's global complex thermal problem.

Acknowledgments

References

Astolfi, M., Binotti, M., Mazzola, S., Zanellato, L., Manzolini, G., 2017. Heliostat aiming point optimization for external tower receiver. Sol. Energy 157, 1114–1129.

Belhomme, B., Pitz-Paal, R., Schwarzbözl, P., Ulmer, S., 2009. A new fast ray tracing tool for high-precision simulation of heliostat fields. J. Sol. Energy Eng. Trans. ASME 131 (3), 0310021–0310028.

Besarati, S.M., Goswami, D.Y., 2014. A computationally efficient method for the design of the heliostat field for solar power tower plant. Sol. Energy 69, 226–232.

Boerema, N., Morrison, G., Taylor, R., Rosengarten, G., 2013. High temperature solar thermal central-receiver billboard design. Sol. Energy 97, 356–368.

Collado, F.J., 2010. One-point fitting of the flux density produced by a heliostat. Sol. Energy 84, 673–684.

Collado, F.J., Guallar, J., 2012. Campo: generation of regular heliostat fields. Renew. Energy 46, 49–59.

Collado, F.J., Guallar, J., 2013. A review of optimized design layouts for solar power tower plants with campo code. Renew. Sustain. Energy Rev. 20, 142–154.

Collado, F.J., Guallar, J., 2016. Two-stages optimised design of the collector field of solar power tower plants. Sol. Energy 135, 884–896.

Collado, F.J, Guallar, J., 2017a Scaling campo code to commercial solar tower plants. In: Proceedings Solar PACES, Santiago de Chile, Chile.

Collado, F.J., and Guallar, J., 2017b. Campo code: a practical framework to design solar tower systems to commercial solar tower plants. In: Proceedings of the 11th International Concentrated Solar Thermal Power Summit CSP Seville 2017, Sevilla, Spain.

Cruz, N.C., Redondo, J.L., Berenguel, M., Alvarez, J.D., Ortigosa, P.M., 2017. Review of software for optical analysing and optimizing heliostat fields. Renew. Sustain. Energy Rev. 72, 1001–1018.

Falcone, P.K., 1986. A handbook for solar central receiver design. SAND86-8009.

Flesch, R., Frantz, C., Maldonado Quinto, D., Schwarzbözl, P., 2017. Towards an optimal aiming for molten salt power towers. Sol. Energy 155, 1273–1281.

Gadalla, M., Saghafifar, M., 2016. Thermo-economic and comparative analyses of two recently proposed optimization approaches for circular heliostat fields: Campo radial-staggered and biomimetic spiral. Sol. Energy 136, 197–209.

Kistler, B.L., 1986. A user's manual for DELSOL3: a computer code for calculating the optical performance and optimal system design for solar thermal central receiver plants. SAND86-8018.

Kolb, J.G., 2011. An evaluation of possible next-generation high-temperature molten-salt power towers. SAND2011-9320.

Meinecke, W., 1982. IAS-RL-100200-028. Almería, Spain.

Lata, J., Alcalde, S., Fernandez, D., Lecube, X., 2010. First surrounding field of heliostats in the world for commercial solar power plant-Gemasolar. In: Proceedings SolarPACES, Perpignan, France.

New Energy Update: CSP, 2018. < http://analysis.newenergyupdate.com/csp-today > .

NREL-SolarPACES, 2018. < https://www.nrel.gov/csp/solarpaces/power_tower.cfm > .

NREL, 2018. SolarPilot (free download at < https://www.nrel.gov/csp/solarpilot.html >).

NREL, 2018. System Advisory Model (SAM) (free download at < https://sam.nrel.gov >).

Relloso, S., Garcia, E., 2015. Tower technology cost reduction approach after Gemasolar experience. Energy Procedia 69, 1660–1666.

Relloso, S., Gutiérrez, Y., 2016. SENER molten salt tower technology. Ouarzazate NOOR III case. In: Al Obaidli, A., et al. (Eds.), SolarPACES 2016, AIP Conference Proceedings 1850 (American Institute of Physics, Melville, NY, 2017), No.030041.

Rodriguez-Sanchez, M.R., Marugan-Cruz, C., Acosta-Iborra, A., Santana, D., 2014. Comparison of simplified heat transfer models and CFD simulations for molten salt external receiver. Appl. Therm. Eng. 73, 991–1003.

Sanchez-Gonzalez, M.R., Santana, D., 2015. Solar flux distribution on central receivers: a projection method from analytic function. Renew. Energy 74, 576–587.

Sanchez-Gonzalez, M.R., Rodriguez-Sanchez, M.R., Santana, D., 2017. Aiming strategy model based on allowable flux densities for molten salt central receivers. Sol. Energy 157, 1130–1144.

Schwarzbözl, P., Schmitz, M., Pitz-Paal, R., 2009. Visual HFLCAL–a software tool for layout and optimization of heliostat fields. In: Proceedings SolarPACES, Berlin, Germany.

Schmitz, M., Schwarzbözl, P., Buck, R., Pitz-Paal, R., 2006. Assessment of the potential improvement due to multiple apertures in central receiver systems with secondary concentrators. Sol. Energy 80, 111–120.

Singer, C., Buck, R., Pitz-Paal, R., Müller-Steinhagen, H., 2010. Assessment of solar power tower driven ultrasupercritical steam cycles applying tubular central receivers with varied heat transfer media. J. Sol. Energy Eng. 132, 041010/1–041010/12.

Vant-Hull, L.L., 2002. The role of "allowable flux density" in the design and operation of molten-salt solar central receivers. J. Sol. Energy Eng. 124, p.165.

Vant-Hull, L.L., 2012. Central tower concentrating solar power (CSP) systems. Concentrating Solar Power Technology: Principles, Developments and Applications. Woodhead Publishing.

Wendelin, T., Dobos, A., Lewandowski, A., 2013. SolTrace: a ray-tracing code for complex solar optical systems, vol. 303. National Renewable Energy Laboratory, Golden, Colorado. NREL/TP-5500-59163.